

Article

Conductive Zinc-Based Metal–Organic Framework Nanorods as Cathodes for High-Performance Zn-Ion Capacitors

Jinfeng Sun ^{*}, Qian Zhang, Chanjuan Liu, Anning Zhang, Linrui Hou ^{*} and Changzhou Yuan ^{*}

School of Materials Science & Engineering, University of Jinan, Jinan 250022, China; 202121100355@stu.ujn.edu.cn (Q.Z.); 202021201003@stu.ujn.edu.cn (C.L.); 202121201067@stu.ujn.edu.cn (A.Z.)

* Correspondence: mse_sunjf@ujn.edu.cn (J.S.); mse_houlr@ujn.edu.cn (L.H.); mse_yuancz@ujn.edu.cn or ayuancz@163.com (C.Y.)

Abstract: Zinc-ion capacitors (ZICs), combining the merits of both high-energy zinc-ion batteries and high-power supercapacitors, are known as high-potential electrochemical energy storage (EES) devices. However, the research on ZICs still faces many challenges because of the lack of appropriate cathode materials with robust crystal structures and rich channels for stable and fast Zn^{2+} ion transport. In this study, we synthesized a robust, conductive, two-dimensional metal–organic framework (MOF) material, zinc-benzenehexathiolate (Zn-BHT), and investigated its electrochemical performance for zinc storage. Zn^{2+} ions could insert into/extricate from the host structure with a high diffusion rate, enabling the Zn-BHT cathode to exhibit a surface-controlled charge storage mechanism. Due to its unique structure, Zn-BHT exhibited a good reversible discharge capacity approaching 90.4 mAh g^{-1} at 0.1 A g^{-1} , as well as a desirable rate capability and good cycling performance. In addition, a ZIC device was fabricated using the Zn-BHT cathode and a polyaniline-derived porous carbon (PC) anode, which depicted a high working voltage of up to 1.8 V and a high energy density of $\sim 37.2 \text{ Wh kg}^{-1}$. This work shows that conductive MOFs are high-potential electrode materials for ZICs and provide new enlightenment for the development of electrode materials for EES devices.

Keywords: zinc-ion capacitors; cathode materials; conductive MOFs; Zn-benzenehexathiolate; electrochemical performance



Citation: Sun, J.; Zhang, Q.; Liu, C.; Zhang, A.; Hou, L.; Yuan, C. Conductive Zinc-Based Metal–Organic Framework Nanorods as Cathodes for High-Performance Zn-Ion Capacitors. *Batteries* **2024**, *10*, 222. <https://doi.org/10.3390/batteries10070222>

Academic Editor: Yong-Joon Park

Received: 30 April 2024

Revised: 12 June 2024

Accepted: 20 June 2024

Published: 24 June 2024



Copyright: © 2024 by the authors. Licensee MDPI, Basel, Switzerland. This article is an open access article distributed under the terms and conditions of the Creative Commons Attribution (CC BY) license (<https://creativecommons.org/licenses/by/4.0/>).

1. Introduction

As the demand for electricity increases in our daily life, it is very attractive to search for electrical energy storage (EES) systems with high performance, reliability, and economy [1–3]. Lithium-ion batteries (LIBs) have been recognized as one of the most successful system thanks to their high energy density, good rate capability, and low self-discharge rate [4,5], and have been commercially used in electric vehicles and electronic products. Nevertheless, limited lithium resources and highly flammable organic electrolytes that may lead to serious safety issues of LIBs have prohibited their large-scale application [6]. To address these problems, plenty of research has focused on the exploration of EES devices with low cost and high safety [7–10].

Among various EES systems, zinc-ion capacitors (ZICs) have gained considerable interest. Firstly, the use of aqueous electrolytes rather than organic electrolytes makes for the high safety and biocompatibility of ZICs [11,12]. Secondly, unlike Li^{+} -, Na^{+} -, and K^{+} -based EES systems, ZICs based on multivalent Zn^{2+} can provide double-electron transport with one mole of reacted ions, resulting in higher energy densities [13]. Previous studies have already confirmed the concept and great potential of ZICs using MnO_2 as a cathode material and activated carbon (AC) as an anode material, which can alleviate Zn dendrites of metallic Zn anodes [14]. However, the poor rate and cycling performance due to the manganese dissolution and irreversible formation–dissolution of $Zn_4(OH)_6SO_4 \cdot nH_2O$ on the cathode still limits their practical application. Moreover, the high polarity of Zn^{2+}

frequently causes stronger electrostatic interactions with the cathodic host, leading to slower diffusion kinetics [15,16]. Therefore, appropriate cathode materials with stable crystal structure and rich channels are crucial for the further development of ZICs with good rate performance and cycling stability.

So far, a variety of cathode materials have been investigated, such as Prussian blue analogs, vanadium-based (VO_x) and manganese-based oxides (MnO_x), and organic compounds, for Zn ion storage [17–20]. However, these materials do not exhibit sufficient electrochemical performance for Zn^{2+} storage. For examples, $\alpha\text{-MnO}_2$ with a 2×2 tunneling structure could afford large tunnels for the fast diffusion of Zn^{2+} ions within the primary structure, affording high capacity and rate capability [21]. However, these materials always suffer from low cyclic stability attributed to the ineluctable dissolution, large volume change, and unstable phase transition of MnO_x [19,21]. Although VO_x -based cathodes can offer high capacity and excellent rate capability, they are usually associated with high cost and toxicity, as well as the dissolution of vanadium [18,22].

Due to their structural diversity, ultra-high specific surface area ($\geq 7000 \text{ m}^2 \text{ g}^{-1}$), adjustable pore structure, and molecular-level modulation, metal–organic frameworks (MOFs) have gained great attention in the area of energy conversion and storage [23–26]. Even more encouraging, intrinsically conductive MOFs have been developed in recent years and quickly draw researchers' attention [25,27–29]. Sheberla et al. reported the fabrication of $\text{Ni}_3(2,3,6,7,10,11\text{-hexylaminotriphenyl})_2$ ($\text{Ni}_3(\text{HITP})_2$) as electrode materials for supercapacitors [25]. The fabricated devices depicted high area capacitance and excellent cycling performance. After that, conductive MOFs prepared from hexaaminobenzene (HAB) ligands ($\text{Cu-}/\text{Ni-HAB}$) were studied as active material for supercapacitors, presenting a high area capacitance of 20 F cm^{-2} and extraordinary electrochemical stability [28]. Recently, Nam et al. reported the use of $\text{Cu}_3(2,3,6,7,10,11\text{-hexahydroxytriphenylene})_2$ ($\text{Cu}_3(\text{HHTP})_2$) as cathode material for Zn^{2+} storage, which reached a high capacity of 228 mAh g^{-1} at 50 mA g^{-1} and maintained $\sim 75\%$ of its initial capacity after 500 cycles [29]. Notably, even at a high rate of 4000 mA g^{-1} ($\sim 18 \text{ C}$), $\text{Cu}_3(\text{HHTP})_2$ provided a high capacity of 124.4 mAh g^{-1} . From the foregoing, conductive MOFs are highly promising electrode materials for EES devices. Nevertheless, the current research and application of conductive MOF materials for Zn^{2+} storage is still in the exploratory stage, and further exploration is needed.

Herein, we designed and synthesized a new and novel conductive zinc-benzenehexathiolate (Zn-BHT) MOF material through a facile and mild process and first investigated the electrochemical performance as a cathode material for ZICs. For the obtained Zn-BHT conjugated coordination polymer, each sulfur atom of the BHT linker was coordinated with two Zn^{2+} ions in the 2D plane, forming an extended $\pi\text{-}d$ conjugated conductive framework. The electrochemical tests showed that Zn^{2+} insertion and extraction reactions are highly reversible in the Zn-BHT electrode. The reaction of Zn^{2+} ions with Zn-BHT occurs reversibly at approximately 1.39 V and 0.48 V (vs. Zn/Zn^{2+}), respectively. Furthermore, a ZIC was fabricated based on the Zn-BHT cathode and polyaniline-derived porous carbon (PC) anode, which delivered a high specific energy density of 37.2 Wh kg^{-1} at 90.5 W kg^{-1} , and a superior cycle performance with a capacity retention value of 150% after 1800 cycles at 0.1 A g^{-1} . This conductive Zn-BHT MOF material with good rate performance and stable reversible capacity is a promising cathode material for Zn^{2+} -based EES devices.

2. Materials and Methods

2.1. Materials

KOH (AR), ZnCl_2 (98%), and $(\text{NH}_4)_2\text{S}_2\text{O}_8$ (AR) were purchased from Sinopharm Group Chemical reagent Co., LTD (Shanghai, China). Aniline ($\geq 99.9\%$) was bought from Shanghai Aladdin Biochemical Technology Co., LTD (Shanghai, China) and HCl (37 wt%) was purchased from Yantai Far East Fine Chemical Co., LTD (Yantai, China). Benzenehexathiol (95%) was purchased from Mackin Biochemical Co., LTD (Shanghai, China).

2.2. Synthesis of Zn-BHT and PC

A total of 75.7 mg of $ZnCl_2$ was added to a degassed methanol solvent (100 mL) under a nitrogen atmosphere to form a transparent solution. Next, 50 mg of BHT powder was slowly added into the above solution within 30 min. Then, the mixture was placed at room temperature to react for 24 h. The resulting powder was collected, filtered, and washed with deionized water and ethanol. After drying at 100 °C under vacuum for 12 h, Zn-BHT was obtained with a yield of ~73 mg (~85%).

PC was synthesized through a two-step heat treatment process using polyaniline (PANI) as the carbon source and KOH as the activating agent, according to a previous reported study [30].

2.3. Material Characterization

A field emission scanning electron microscope (FESEM, JEOL-6300F, Japan) and transmission electron microscope (TEM, JEOL JEM-2100, FEI) were utilized to observe the morphologies and microstructures of the synthesized samples. Powder X-ray diffraction (XRD, Rigaku Ultima IV, Japan) and Raman spectra (Renishaw1000B Raman spectrometer) were recorded to explore the phase structure of Zn-BHT. The surface chemical species and valence state of Zn-BHT and PC were examined by X-ray photoelectron spectroscopy (XPS, ESCALAB 250Xi, USA). The Brunauer–Emmett–Teller (BET) surface area and pore size distribution data were collected by N_2 adsorption/desorption tests at 77 K using Quantachrome (NOVA 2000, USA).

2.4. Electrode Preparation and Electrochemical Measurement

For half cells, the synthesized Zn-BHT powder was ground with carbon black and polyvinylidene fluoride (PVDF) at a ratio of 7:2:1 and further ground by adding an appropriate amount of N-methyl pyrrolidone (NMP). The resulting slurry was coated on the pre-weighed carbon paper (~12 mm diameter, ~0.1 mm thick) and vacuum dried for 12 h. The mass loading in each electrode was 0.8–1.2 mg cm^{-2} . The resulting electrode sheet was assembled with metallic zinc foil under an aqueous electrolyte using 2016 coin-type cells.

As regards the PC anode electrode, PC, carbon black, and PVDF with a mass ratio of 8:1:1 were thoroughly mixed in NMP and coated on stainless steel mesh (300 mesh). The ZIC device was fabricated using Zn-BHT as the cathode and a PC electrode as the anode, a glass fiber filter as the separator, and 3 M $Zn(CF_3SO_3)_2$ as the electrolyte.

Galvanostatic charge/discharge (GCD) was tested by a LAND test system (Land CT2001A). Cyclic voltammetry (CV) measurements were performed on an IVIUM electrochemical workstation (The Netherlands). The energy/power density of the ZICs were calculated according to following equations:

$$P = \Delta V \times i/m \quad (1)$$

$$E = P \times t/3600 \quad (2)$$

$$\Delta V = (V_{max} + V_{min})/2 \quad (3)$$

where i , t and m are the discharge current (A), the discharge time (s), and the total mass of active materials (kg), respectively. V_{max} and V_{min} are the voltages at the beginning and end of the discharge (V).

3. Results

3.1. Structure Characterization of Zn-BHT

Zn-BHT was obtained by the reaction of BHT with $ZnCl_2$ in degassed methanol under a nitrogen atmosphere for 24 h at room temperature. As depicted in Figure 1, each sulfur atom of the BHT was fitted to two Zn^{2+} ions in the 2D plane to obtain an extended $\pi-d$ conjugated conductive framework, and the 2D planes were stacked together with a layer spacing of 0.35 nm. The micromorphology of the synthesized Zn-BHT products was

characterized by FESEM and TEM, as shown in Figure 2. It can be observed that the sample exhibits a uniform microrod structure with a smooth surface. The length of these rods extends a few micrometers with diameters of about 300–400 nm (Figure 2a). The TEM result further confirms the microrod morphology of Zn-BHT (Figure 2b). The high-resolution TEM image presented in Figure 2c shows that the crystal lattice spacing of the Zn-BHT is 0.35 nm. The selected area electron diffraction (SAED) pattern revealed the polycrystal structure of Zn-BHT. In addition, energy-dispersive X-ray spectroscopy (EDX) analysis was performed to further demonstrate the chemical composition of the synthesized Zn-BHT, which depicts the uniformly distributed C, S, and Zn throughout the rod (Figure 2d).

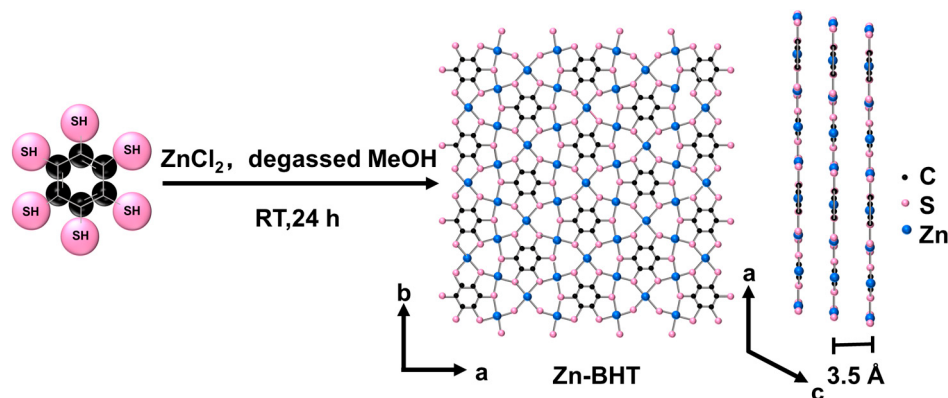


Figure 1. Synthesis process of 2D Zn-BHT MOF (MeOH = methanol, RT = room temperature).

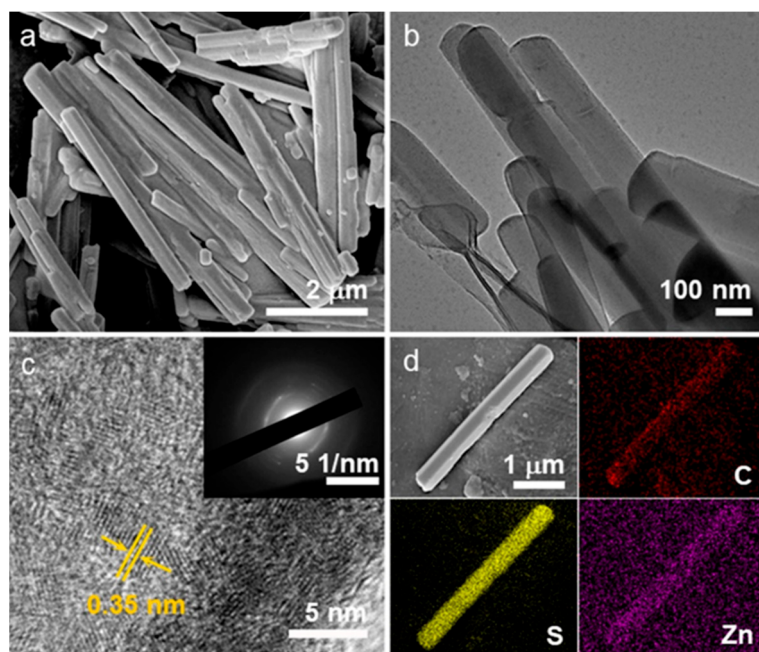


Figure 2. (a) SEM, (b) TEM, (c) high-resolution TEM images (inset corresponds to the SAED pattern), and (d) SEM-EDX mapping of C, S, and Zn elements of the obtained Zn-BHT microrods.

XRD was conducted to qualitatively analyze the crystal structure and phase composition of Zn-BHT, as presented in Figure 3a. Several characteristic diffraction peaks of Zn-BHT are observed at 11.4° , 25.6° , 31.1° , and 32.8° in the XRD pattern, which resemble that of Ni_3BHT and are different from the reported Ni_3BHT_2 [31,32]. Thus, we speculate that the structural formula of the material is Zn_3BHT . No impurity peaks appear, which indicates the successful synthesis of Zn-BHT with good crystallinity and high purity. The structure of these samples was further verified using Raman measurement (Figure 3b). The peaks at

886 and 1145 cm^{-1} are the characterized peaks of C-S bonds. Peaks at 383 and 1490 cm^{-1} can be ascribed to Zn-S and C-C, respectively. Meanwhile, the signal at 2500 cm^{-1} belongs to the S-H stretching vibration, which may be attributed to the incomplete coordination between Zn ions and thiol groups [33]. The XPS survey spectra show the presence of Zn, S, C, and O elements (Figure 3c). The high-resolution Zn 2p spectrum of Zn-BHT was divided into two separate peaks at 1022.2 and 1045.3 eV (Figure 3d), corresponding to the Zn 2p_{3/2} and Zn 2p_{1/2} orbitals, respectively. In the high-resolution S 2p spectrum, the S 2p peaks in the XPS spectrum at 161 and 165 eV could be split into two pairs of doublet peaks, assignable to the sulfur atoms that appeared in the Zn-BHT framework (163.2 and 164.4 eV) and the sulfur atoms from BHT (162.5 and 163.7 eV), as shown in Figure 3e [34]. In addition, due to the spin-orbit coupling effect, each S 2p component split into a doublet structure of S 2p_{3/2} and S 2p_{1/2}, with a binding energy difference of 1.2 eV [35]. Meanwhile, the C 1s spectra shown in Figure 3f were deconvoluted into three distinct peaks at 284.8, 286.5, and 288.6 eV, corresponding to C₆ ring, C-S, and C-O, respectively. In brief, all of the above results prove the successful synthesis of the Zn-BHT MOF material.

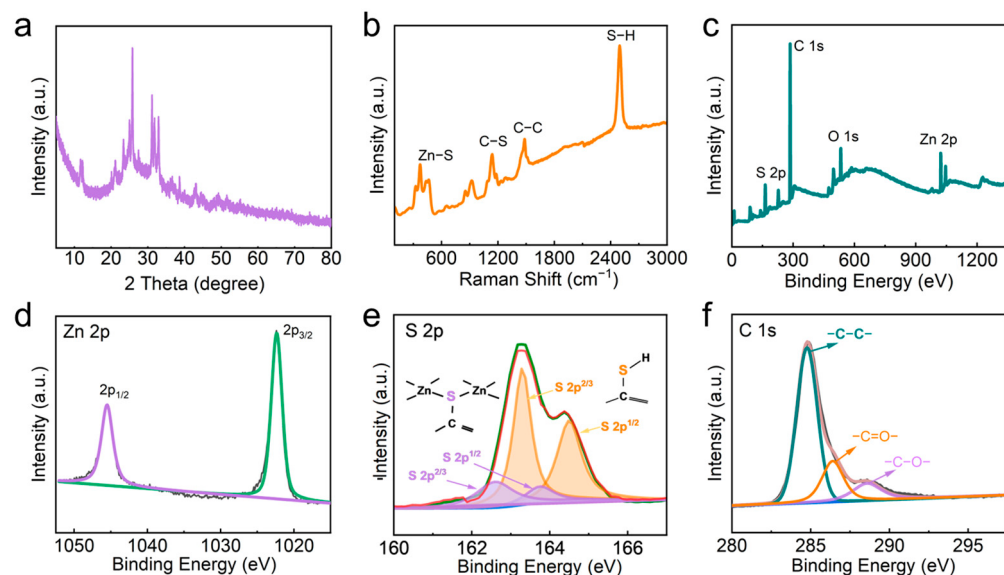


Figure 3. Structural characterization of the obtained Zn-BHT microrods. (a) XRD. (b) Raman. (c) XPS survey spectra. High-resolution XPS spectra of (d) Zn 2p, (e) S 2p, and (f) C 1s.

3.2. Electrochemical Properties of Zn-BHT

The CV test was carried out at 0.2 mV s^{-1} within a potential window of 0.2–1.6 V (vs. Zn/Zn²⁺) to investigate the Zn²⁺-storage performance of the Zn-BHT electrode. CVs of Zn-BHT on carbon paper in 3.0 M aqueous solution of Zn(CF₃SO₃)₂ (Figure 4a) show that the Zn²⁺ insertion and extraction reactions are reversible. During the first charge process, an evident oxidation peak at ~1.38 V (vs. Zn/Zn²⁺) was observed and disappeared in the subsequent cycles. The reaction of Zn²⁺ ions with Zn-BHT occurs reversibly at approximately 1.39 V and 0.48 V (vs. Zn/Zn²⁺), respectively. The second and third curves almost coincide, indicating the high reversibility of the intercalation/deintercalation of Zn²⁺ in Zn-BHT. GCD tests showed that this reversibility was also reflected in the charge/discharge curves (Figure 4b). At a current density of 100 mA g^{-1} , a reversible discharge capacity of 90.4 mAh g^{-1} was obtained. Notably, the initial coulomb efficiency of the electrode is 42% with a charge capacity of 212 mAh g^{-1} . Figure S1 depicts the morphology of the electrode after the GCD test. The surface of the Zn-BHT electrode after cycling is covered by a thick film, which may be attributed to the irreversible reaction between the active material and the electrolyte or the collapse of the loose structure after the first charge-discharge process [36]. After that, the third GCD curve is in perfect agreement with the second GCD curve, indicating that the Zn²⁺ storage is stable and reversible. The

rate performance of the Zn-BHT electrode was tested at current densities from 100 mA g^{-1} to 2000 mA g^{-1} (Figure 4c). With the increase in current density, the capacity decreases gradually. At 1 A g^{-1} , Zn-BHT delivered a capacity retention of 28.1% compared with the initial capacity at 100 mA g^{-1} . Add, with cycling, the CE of the electrode was gradually increased to approximately 100%. The typically reported MOF-based cathode materials including CuHCF [37], ZnHCF [24], PBA [38], $\text{Cu}_3(\text{HHTP})_2$ [29], and Mn(BTC) [39] are also listed for comparison (Figure 4d). Due to the good conductivity of Zn-BHT, this value exceeds most reported traditional MOF materials for Zn^{2+} storage, indicating its potential in EESs, although this value is still inferior to the conductive $\text{Cu}_3(\text{HHTP})_2$ cathodes and V-based oxide cathodes. In addition, the Zn-BHT electrode showed good stability, which is gradually increased with cycling (Figure 4e). This may be ascribed to the gradually improved electrochemical activity of the electrode [40].

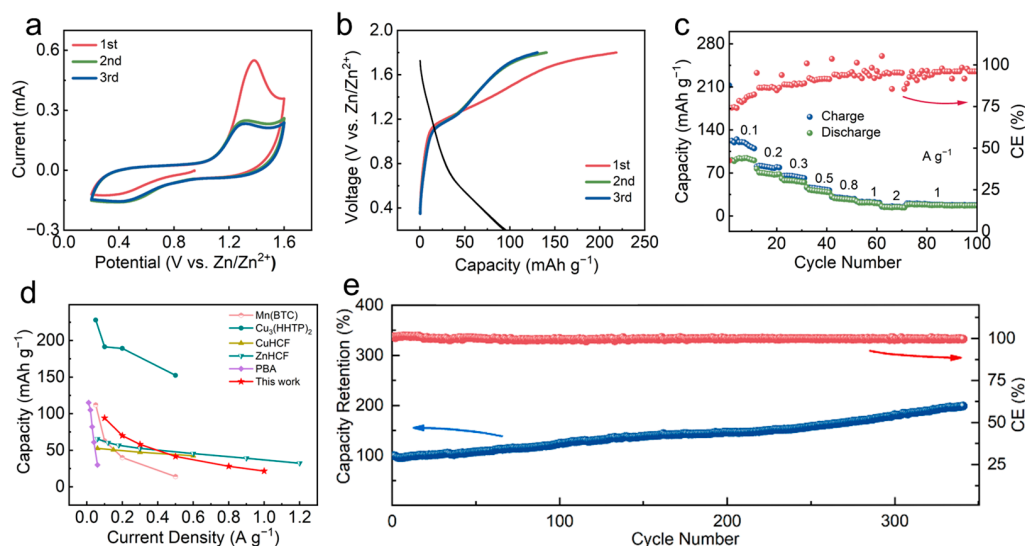


Figure 4. Electrochemical properties of Zn-BHT. (a) CV curves at 0.2 mV s^{-1} . (b) GCD curves at 100 mA g^{-1} . (c) Rate performance. (d) Comparison of specific capacities of Zn-BHT with previously reported MOF-based cathode materials. (e) Cyclic stability at 100 mA g^{-1} after ten cycles of activation.

For a better understanding of the electrochemical kinetics of Zn-BHT, CV curves at different scan rates from 0.2 to 1 mV s^{-1} are given in Figure 5a. As the scan rate increases, the response currents increase and the CV curves maintain their shapes with slight deviations, indicating the fast insertion kinetics of Zn^{2+} in Zn-BHT [41]. The relationship between the response current i (mA) and the scan rate v (mV s^{-1}) can be interpreted as the following equation [42]:

$$i = av^b \quad (4)$$

where a and b are adjustable parameters. When the b value is 0.5 , this means that the charge storage process is controlled by ion diffusion. And when the b value is 1 , this means that the charge storage is a fully surface-controlled process. As presented in Figure 5b, the specific b values were calculated to be 0.87 and 0.83 , corresponding to the pair of redox peaks, respectively. This shows that the charging and discharging processes are controlled by both ion diffusion and pseudo-capacitive behavior. Moreover, the pseudo-capacitance contribution ratios at different scan rates have been calculated according to the following equation [30]:

$$i = k_1v + k_2v^{1/2} \quad (5)$$

where k_1v and $k_2v^{1/2}$ corresponded to the pseudo-capacitance contribution and the diffusion-controlled contribution, respectively. By fitting data of k_1v and $k_2v^{1/2}$, the capacitive contribution is quantified as 76% at 1 mV s^{-1} , demonstrating that the total energy storage in the Zn-BHT electrode mostly results from the capacitive process (Figure 5c). Moreover,

the pseudo-capacitance contribution of Zn-BHT was calculated to be 50%, 52.8%, 60.1%, 69.3%, and 76% at the scan rates of 0.2, 0.3, 0.5, 0.8, and 1 mV s⁻¹, respectively (Figure 5d). The above results reflect that with the scan rate increase, the electrochemical reaction is gradually mainly controlled by capacitive processes rather than diffusion. The good electronic conductivity and novel structure of Zn-BHT could be responsible for the good rate capability, indicating the great potential of Zn-BHT as cathode materials for ZICs.

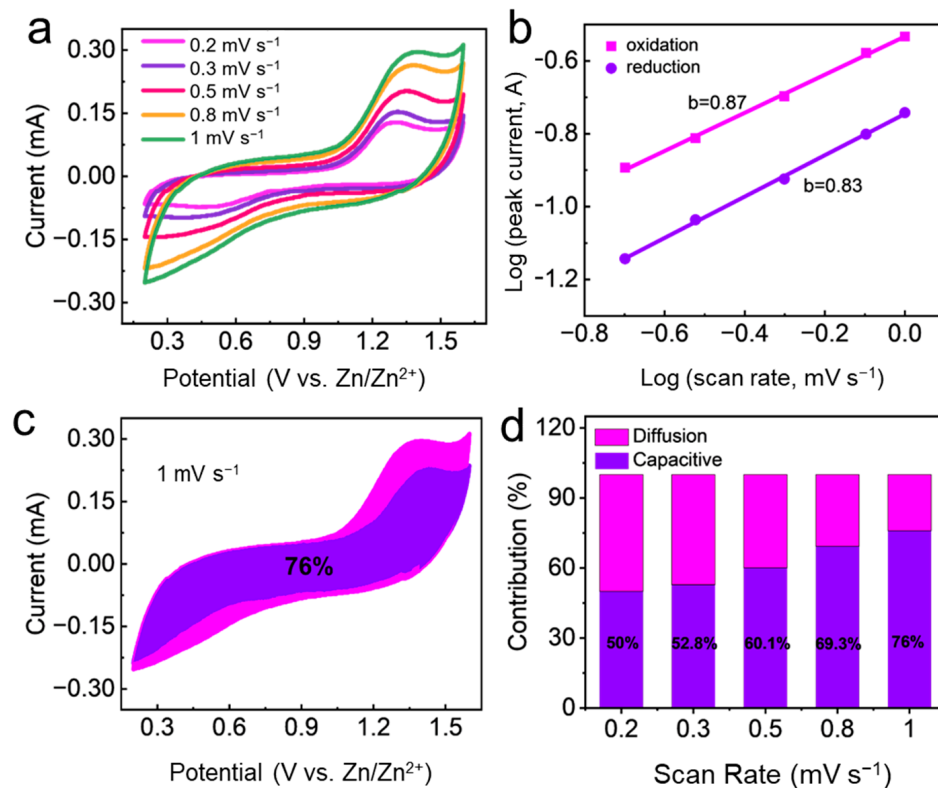


Figure 5. Electrochemical kinetic exploration of Zn-BHT cathode. (a) CV curves at different scanning rates. (b) Mathematical relationship of $\log(i)$ and $\log(v)$ plot. (c) Pseudo-capacitance contribution at 1 mV s⁻¹ (purple part). (d) Pseudo-capacitance contribution at different scan rates.

The diffusion coefficient of Zn²⁺ ($D_{Zn^{2+}}$) can be obtained using the galvanostatic intermittent titration technique (GITT) method. At 100 mA g⁻¹ and a relaxation time and charge/discharge time of 120 s, the $D_{Zn^{2+}}$ was calculated by using the following equation [43]:

$$D_{Zn^{2+}} = \frac{4}{\pi\tau} \left(\frac{n_m V_m}{S} \right)^2 \left(\frac{\Delta E_s}{\Delta E_t} \right)^2 \cdot \left(\tau \ll \frac{L^2}{D_{Zn^{2+}}} \right) \quad (6)$$

where n_m is the number of moles of electrode material, V_m is the molar volume, S is the contact area between the electrode and collector, L is the thickness of the active materials, ΔE_s is the change in potential caused during charging and discharging, and ΔE_t is the potential difference generated during relaxation. Figure 6 shows the GITT curve and the calculated $D_{Zn^{2+}}$ of the Zn-BHT electrode during the charging and discharging processes. The measured $D_{Zn^{2+}}$ by GITT is in the 10^{-13} – 10^{-11} cm² s⁻¹ order of magnitude, indicating decent kinetics due to the good conductivity of Zn-BHT.

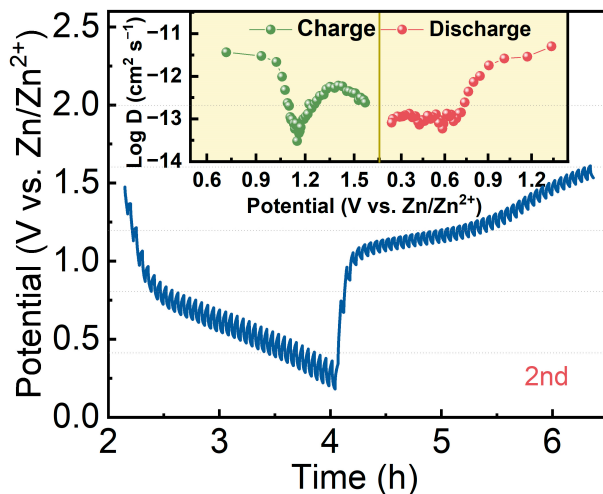


Figure 6. GITT curve for Zn-BHT cathode, and $D_{Zn^{2+}}$ values during charge/discharge process (the inset).

3.3. Electrochemical Properties of Fabricated ZIC

To evaluate the practical application of the Zn-BHT electrode as a cathode for ZICs, we assembled a ZIC full cell using PC as the anode electrode. The PC was synthesized by the pyrolysis of PANi nanorods (Figure S2a,b) following a previously reported method [30]. The SEM image of PC (Figure S2c,d) shows a typical porous structure. The XRD pattern (Figure S3) of PC shows a broad diffraction peak at about 23° , corresponding to the (002) plane of graphite, which proves the amorphous structure characteristics of the carbon material. The specific surface area (SSA) and pore size distribution information of PC were investigated by N_2 adsorption/desorption measurement, as presented in Figure S4. This isotherm curve with no obvious hysteresis loop conforms to the mixed type of type I and IV isotherms with a high BET surface area of $2677.5\text{ m}^2\text{ g}^{-1}$. The pore size distribution of PC indicates a high portion of micropores with a pore width of $\sim 1.2\text{ nm}$ and a small portion of mesopores in the width range of $2\text{--}4\text{ nm}$. Based on this rich pore structure and large SSA, it will be conducive to ion transport and adsorption, so as to show superior electrochemical performance. Raman spectra and the corresponding Gaussian fit curves of PC are shown in Figure S5. Two characteristic peaks at ~ 1350 and 1582 cm^{-1} are observed, corresponding to the D (disordered carbon or defective graphitic structures) and G (sp^2 bonded carbon atoms) band of the carbon material, respectively. The peak intensity ratio (I_D/I_G) of D and the G band gives an indication of the graphitization degree of the carbon [44]. In general, the lower the I_D/I_G value, the higher the graphitization degree of the carbon material. Furthermore, the I band (1224 cm^{-1}) corresponds mainly to $sp^2\text{-}sp^3$ bonded carbon atoms, while the D'' band (1506 cm^{-1}) is associated with amorphous carbon and the D' band corresponds to graphitic defects [44,45]. PC depicted an I_D/I_G value of 0.93, a relatively small value that would indicate a high degree of graphitization of the synthesized activated carbon with good conductivity.

The ZIC device was assembled by using the Zn-BHT cathode and PC anode with 3 M $Zn(CF_3SO_3)_2$ as electrolyte, which is schematically presented in Figure 7a. The mass ratio of PC to Zn-BHT is optimized as ~ 1.5 to realize the charge balance of the two electrodes here. During the discharging process, Zn^{2+} is inserted into the Zn-BHT while the anions are absorbed by PC. Figure 7b presents the CV curves of the fabricated Zn-BHT//PC ZIC device at different scan rates within a working voltage of $0.01\text{--}1.8\text{ V}$. At a small sweep scan of 5 mV s^{-1} , the CV delivers an obvious rectangular shape, indicating the typical capacitive behavior. Moreover, with the increase in the scan rate, the rectangular shape of the CV curves is still maintained with slight deviation. Figure 7c shows the GCD curves of the fabricated ZIC under various current densities. Similar to the CV results, the GCD curves depicted typical capacitive behavior with symmetric inverted triangular shapes. At current

densities of 0.1, 0.2, 0.5, 0.8, and 1 A g^{-1} , the corresponding specific capacities are about 37.6, 24.6, 15.1, 12.2 and 10.8 F g^{-1} , respectively. The results show that the Zn-BHT//PC device can adapt to the fast charging and discharging process at large current densities. In addition, the energy density of such a ZIC device is about 37.15 Wh kg^{-1} when the power density is 90.5 W kg^{-1} , and even at a power density of 905 W kg^{-1} , the energy density can be maintained at $\sim 12 \text{ Wh kg}^{-1}$. Although the fabricated ZIC device depicts a relatively lower energy density than most ZICs based on Zn anodes, the energy density value is higher than some reported ZICs based on AC anodes (Figure 7d) [14,46–48], as well as the latest aqueous Li/Na ion capacitors (e.g., 11.5 Wh kg^{-1} for LFP@C//ARGO Li-ion capacitors [49], and 27.9 Wh kg^{-1} for MnHCF//Fe₃O₄/rGO Na-ion capacitors [50]).

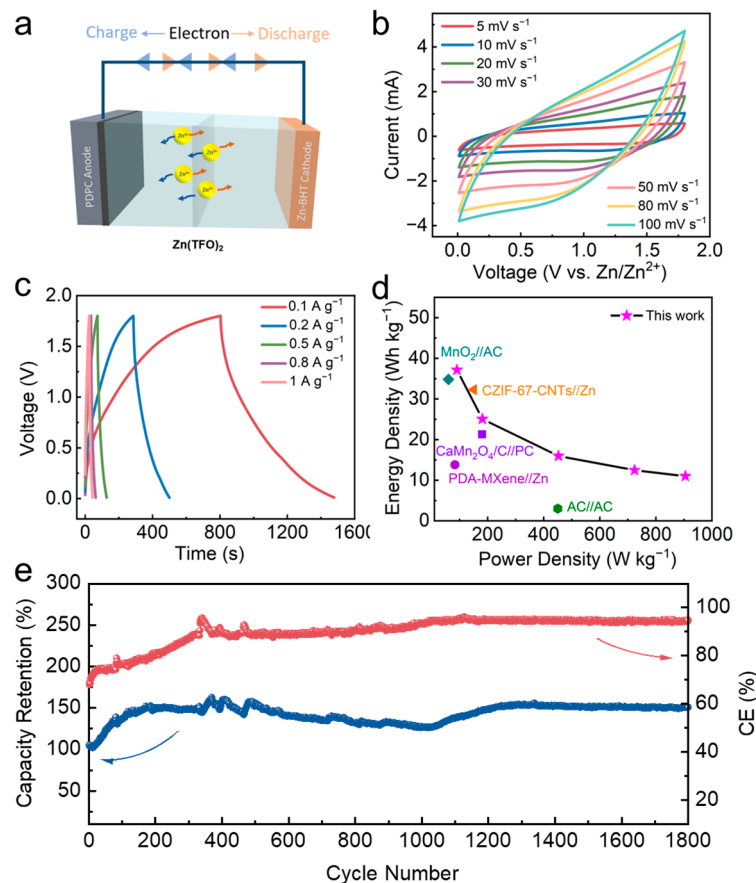


Figure 7. Electrochemical performance of the assembled Zn-BHT//PC ZIC. (a) Schematic configuration. (b) CV profiles from 5 to 100 mV s^{-1} . (c) GCD curves from 0.1 to 2 A g^{-1} . (d) Ragone plot showing the comparison of this work with reported studies. (e) Long-term cycling performance at 0.1 A g^{-1} .

The good charging and discharging performance of Zn-BHT//PC can be ascribed to the following aspects: Firstly, the good electrical conductivity and layered structure of the Zn-BHT cathode can facilitate the insertion/de-insertion of Zn²⁺, resulting in fast charge transfer kinetics, which may effectively alleviate the kinetics mismatch problem between negative and positive electrodes. Secondly, the large SSA and highly porous structure of the PC anode increase the contact area between the electrolyte and the electrode, which is conducive to the transport and adsorption/desorption of ions. Finally, a suitable ratio of positive and negative electrodes also contributes to the good electrochemical performance of the ZIC. In addition, the Zn-BHT//PC device also demonstrates a long service life, as shown in Figure 7e. Under 0.1 A g^{-1} , the capacity retention of about $\sim 150\%$ was obtained after 1800 charging and discharging cycles.

4. Conclusions

In conclusion, we synthesized a novel 2D conductive MOF material, Zn-BHT, through a facile and mild reaction between BHT and ZnCl_2 in deoxygenated methanol for 24 h and first investigated the Zn^{2+} storage performance as a cathode for ZICs. Due to its unique layered structure and good conductivity, the insertion/de-insertion of Zn^{2+} ions is highly reversible in the Zn-BHT electrode with a high diffusion rate. A discharge capacity of 90.4 mAh g^{-1} was obtained at 0.1 A g^{-1} , as well as good rate performance and cyclic stability. Moreover, the ZIC device was successfully fabricated using the Zn-BHT cathode and PC anode, which exhibited a specific energy density of $\sim 37.2 \text{ Wh kg}^{-1}$ and a long-term cycle life with a capacity retention value of $\sim 150\%$ after 1800 cycles at 0.1 A g^{-1} . This work shows that Zn-BHT is a promising cathode material for Zn^{2+} storage. Although further research to obtain an in-depth understanding of the Zn^{2+} storage mechanisms of conductive MOFs is needed, this study provides new guidance for the development of high-capacity and high-power conductive MOFs for ZIC cathodes.

Supplementary Materials: The following supporting information can be downloaded at <https://www.mdpi.com/article/10.3390/batteries10070222/s1>: Figure S1: SEM images of the post-cyclic Zn-BHT electrode; Figure S2: SEM images of the (a,b) synthesized PANi and (c,d) PC; Figure S3: XRD pattern of PC; Figure S4: (a) Nitrogen adsorption and desorption isotherm and (b) pore size distribution calculated using DFT method of PC; Figure S5: Raman spectra of PC.

Author Contributions: Conceptualization, L.H. and C.Y.; investigation, Q.Z., C.L. and A.Z.; data curation, Q.Z., C.L. and A.Z.; writing—original draft preparation, J.S., C.L. and Q.Z.; writing—review and editing, J.S., C.L. and Q.Z.; supervision, L.H. and C.Y.; project administration, L.H. and C.Y. All authors have read and agreed to the published version of the manuscript.

Funding: This research was funded by the National Natural Science Foundation of China (No. U22A20145, 52072151, 52171211, 52271218), the Jinan Independent Innovative Team (2020GXRC015), the Major Program of the Shandong Province Natural Science Foundation (ZR2023ZD43, ZR2021ZD05), and the Science and Technology Program of the University of Jinan (XKY2119).

Data Availability Statement: The raw data supporting the conclusions of this article will be made available by the authors on request.

Conflicts of Interest: The authors declare no conflicts of interest.

References

1. Blanc, L.E.; Kundu, D.; Nazar, L.F. Scientific challenges for the implementation of Zn-ion batteries. *Joule* **2020**, *4*, 771–799. [[CrossRef](#)]
2. Sun, J.; Liu, C.; Song, X.; Zhang, J.; Liu, Y.; Liang, L.; Jiang, R.; Yuan, C. Electrochemical energy storage devices under particular service environments: Achievements, challenges, and perspective. *Appl. Phys. Rev.* **2022**, *9*, 031301. [[CrossRef](#)]
3. Liu, Z.; Huang, Y.; Huang, Y.; Yang, Q.; Li, X.; Huang, Z.; Zhi, C. Voltage issue of aqueous rechargeable metal-ion batteries. *Chem. Soc. Rev.* **2020**, *49*, 180–232. [[CrossRef](#)] [[PubMed](#)]
4. Choi, J.W.; Aurbach, D. Promise and reality of post-lithium-ion batteries with high energy densities. *Nat. Rev. Mater.* **2016**, *1*, 1–16. [[CrossRef](#)]
5. Manthiram, A. A reflection on lithium-ion battery cathode chemistry. *Nat. Commun.* **2020**, *11*, 1550. [[CrossRef](#)] [[PubMed](#)]
6. Lu, L.; Han, X.; Li, J.; Hua, J.; Ouyang, M. A review on the key issues for lithium-ion battery management in electric vehicles. *J. Power Sources* **2013**, *226*, 272–288. [[CrossRef](#)]
7. Li, W.; Dahn, J.R.; Wainwright, D.S. Rechargeable lithium batteries with aqueous electrolytes. *Science* **1994**, *264*, 1115–1118. [[CrossRef](#)]
8. Luo, J.; Cui, W.; He, P.; Xia, Y. Raising the cycling stability of aqueous lithium-ion batteries by eliminating oxygen in the electrolyte. *Nat. Chem.* **2010**, *2*, 760–765. [[CrossRef](#)]
9. Deng, Q.; Liu, F.; Wu, X.; Li, C.; Zhou, W.; Long, B. An aqueous BiI_3 -Zn battery with dual mechanisms of Zn^{2+} (de)intercalation and I^-/I_2 redox. *J. Energy Chem.* **2024**, *89*, 670–678. [[CrossRef](#)]
10. Zhou, H.; Li, X.; Li, Y.; Zheng, M.; Pang, H. Applications of M_xSe_y ($\text{M} = \text{Fe}, \text{Co}, \text{Ni}$) and their composites in electrochemical energy storage and conversion. *Nano-micro Lett.* **2019**, *11*, 40. [[CrossRef](#)]
11. Zhang, Y.; Wan, F.; Huang, S.; Wang, S.; Niu, Z.; Chen, J. A chemically self-charging aqueous zinc-ion battery. *Nat. Commun.* **2020**, *11*, 2199. [[CrossRef](#)]

12. Zhao, Y.; Zhu, Y.; Zhang, X. Challenges and perspectives for manganese-based oxides for advanced aqueous zinc-ion batteries. *Infomat.* **2020**, *2*, 237–260. [[CrossRef](#)]
13. Chen, L.; Liu, F.; Dong, Y.; Pei, Y.; Wang, X.; Wu, X.; Zheng, X.; He, W.; Long, B. Anion-induced facet-selective etching of Zn metal anode for long cycle aqueous Zn-ion batteries. *J. Energy Storage* **2024**, *87*, 111529. [[CrossRef](#)]
14. Ma, X.; Cheng, J.; Dong, L.; Liu, W.; Mou, J.; Zhao, L.; Wang, J.; Ren, D.; Wu, J.; Xu, C.; et al. Multivalent ion storage towards high-performance aqueous zinc-ion hybrid supercapacitors. *Energy Storage Mater.* **2019**, *20*, 335–342. [[CrossRef](#)]
15. Zhou, J.; Shan, L.; Wu, Z.; Guo, X.; Fang, G.; Liang, S. Investigation of V₂O₅ as a low-cost rechargeable aqueous zinc ion battery cathode. *Chem. Commun.* **2018**, *54*, 4457–4460. [[CrossRef](#)]
16. Jia, D.; Zheng, K.; Song, M.; Tan, H.; Zhang, A.; Wang, L.; Yue, L.; Li, D.; Li, C.; Liu, J. VO₂·0.2H₂O nanocuboids anchored onto graphene sheets as the cathode material for ultrahigh capacity aqueous zinc ion batteries. *Nano Res.* **2020**, *13*, 215–224. [[CrossRef](#)]
17. Wang, D.; Zhou, Z.; Ma, T.; Zhang, J.; Zhang, Y.; Ma, R.; Zhang, D.; Yan, T. In situ electrochemical Mn vacancies in CoMnHCF for a high level of zinc storage. *Chem. Commun.* **2024**, *60*, 4080–4083. [[CrossRef](#)] [[PubMed](#)]
18. Zhu, K.Y.; Wu, T.; Bergh, W.V.D.; Stefik, M.; Huang, K. Reversible molecular and ionic storage mechanisms in high-performance Zn_{0.1}V₂O₅·nH₂O xerogel cathode for aqueous Zn-ion batteries. *ACS Nano* **2021**, *15*, 10678–10688. [[CrossRef](#)] [[PubMed](#)]
19. Zhang, Q.; Duan, T.; Xiao, M.; Pei, Y.; Wang, X.; Zhi, C.; Wu, X.; Long, B.; Wu, Y. BiOI nanopaper as a high-capacity, long-life and insertion-type anode for a flexible quasi-solid-state Zn-ion battery. *ACS Appl. Mater. Interfaces* **2022**, *14*, 25516–25523. [[CrossRef](#)]
20. Wang, W.; Tang, Y.; Liu, J.; Li, H.; Wang, R.; Zhang, L.; Liang, F.; Bai, W.; Zhang, L.; Zhang, C. Boosting the zinc storage of a small-molecule organic cathode by a desalination strategy. *Chem. Sci.* **2023**, *14*, 9033–9040. [[CrossRef](#)]
21. Kim, S.J.; Zhu, Y.; Wu, D.R.; Sadique, N.; Quilty, C.D.; Wu, L.; Marschilok, A.C.; Takeuchi, K.J.; Takeuchi, E.S. Unraveling the dissolution-mediated reaction mechanism of α-MnO₂ cathodes for aqueous Zn-ion batteries. *Small* **2020**, *16*, 2005406. [[CrossRef](#)] [[PubMed](#)]
22. Liu, H.; Jiang, L.; Cao, B.; Du, H.; Lu, H.; Ma, Y.; Wang, H.; Guo, H.; Huang, Q.; Xu, B.; et al. Van der Waals interaction-driven self-assembly of V₂O₅ nanoplates and MXene for high-performing zinc-ion batteries by suppressing vanadium dissolution. *ACS Nano* **2022**, *16*, 14539–14548. [[CrossRef](#)] [[PubMed](#)]
23. Guo, L.; Sun, J.; Zhang, W.; Hou, L.; Liang, L.; Liu, Y.; Yuan, C. Bottom-up fabrication of 1D Cu-based conductive metal–organic framework nanowires as a high-rate anode towards efficient lithium storage. *ChemSusChem* **2019**, *12*, 5051–5058. [[CrossRef](#)] [[PubMed](#)]
24. Zhang, L.; Chen, L.; Zhou, X.; Liu, Z. Towards high-voltage aqueous metal-ion batteries beyond 1.5 V: The zinc/zinc hexacyanoferrate system. *Adv. Energy. Mater.* **2015**, *5*, 1400930. [[CrossRef](#)]
25. Sheberla, D.; Bachman, J.C.; Elias, J.S.; Sun, C.; Shao-Horn, Y.; Dinca, M. Conductive MOF electrodes for stable supercapacitors with high areal capacitance. *Nat. Mater.* **2017**, *16*, 220–224. [[CrossRef](#)] [[PubMed](#)]
26. Guo, L.; Sun, J.; Wei, J.; Liu, Y.; Hou, L.; Yuan, C. Conductive metal–organic frameworks: Recent advances in electrochemical energy-related applications and perspectives. *Carbon Energy* **2020**, *2*, 203–222. [[CrossRef](#)]
27. Li, W.; Ding, K.; Tian, H.; Yao, M.; Nath, B.; Deng, W.; Wang, Y.; Xu, G. Conductive metal–organic framework nanowire array electrodes for high-performance solid-state supercapacitors. *Adv. Funct. Mater.* **2017**, *27*, 1702067. [[CrossRef](#)]
28. Feng, D.; Lei, T.; Lukatskaya, M.; Park, J.; Huang, Z.; Lee, M.; Shaw, L.; Chen, S.; Yakovenko, A.; Kulkarni, A.; et al. Robust and conductive two-dimensional metal–organic frameworks with exceptionally high volumetric and areal capacitance. *Nat. Energy* **2018**, *3*, 30–36. [[CrossRef](#)]
29. Nam, K.W.; Park, S.S.; Reis, R.D.; Dravid, V.P.; Kim, H.; Mirkin, C.A.; Stoddart, J.F. Conductive 2D metal–organic framework for high-performance cathodes in aqueous rechargeable zinc batteries. *Nat. Commun.* **2019**, *10*, 4948. [[CrossRef](#)]
30. Wang, R.; Wang, S.; Jin, D.; Zhang, Y.; Cai, Y.; Ma, J.; Zhang, L. Engineering layer structure of MoS₂-graphene composites with robust and fast lithium storage for high-performance Li-ion capacitors. *Energy Storage Mater.* **2017**, *9*, 195–205. [[CrossRef](#)]
31. Banda, H.; Dou, J.; Chen, T.; Libretto, N.J.; Chaudhary, M.; Bernard, G.M.; Miller, J.T.; Michaelis, V.K.; Dinca, M. High-capacitance pseudocapacitors from Li⁺ ion intercalation in nonporous, electrically conductive 2D coordination polymers. *J. Am. Chem. Soc.* **2021**, *143*, 2285–2292. [[CrossRef](#)] [[PubMed](#)]
32. Kambe, T.; Sakamoto, R.; Hoshiko, K.; Takada, K.; Miyachi, M.; Ryu, J.H.; Sasaki, S.; Kim, J.; Nakazato, K.; Takata, M.; et al. π-Conjugated nickel bis(dithiolene) complex nanosheet. *J. Am. Chem. Soc.* **2013**, *135*, 2462–2465. [[CrossRef](#)] [[PubMed](#)]
33. Chen, I.; Lu, C.; Su, W. Highly conductive 2D metal–organic framework thin film fabricated by liquid–liquid interfacial reaction using one-pot-synthesized benzenehexathiol. *Langmuir* **2018**, *34*, 15754–15762. [[CrossRef](#)]
34. Wang, Y.; Chiang, C.; Chang, C.; Maeda, H.; Fukui, N.; Wang, I.; Wen, C.; Lu, K.; Huang, S.; Jian, W.; et al. Two-dimensional bis(dithiolene)iron(II) self-powered UV photodetectors with ultrahigh air stability. *Adv. Sci.* **2021**, *8*, 2100564. [[CrossRef](#)] [[PubMed](#)]
35. Liang, X.; Hart, C.; Pang, Q.; Garsuch, A.; Weiss, T.; Nazar, L.F. A highly efficient polysulfide mediator for lithium-sulfur batteries. *Nat. Commun.* **2015**, *6*, 5682. [[CrossRef](#)] [[PubMed](#)]
36. Sun, J.; Guo, L.; Sun, X.; Zhang, J.; Liu, Y.; Hou, L.; Yuan, C. Conductive Co-based metal–organic framework nanowires: A competitive high-rate anode towards advanced Li-ion capacitors. *J. Mater. Chem. A* **2019**, *7*, 24788–24791. [[CrossRef](#)]
37. Trócoli, R.; Mantia, F.L. An aqueous zinc-ion battery based on copper hexacyanoferrate. *ChemSusChem* **2015**, *8*, 481–485. [[CrossRef](#)] [[PubMed](#)]
38. Liu, Z.; Pulletikurthi, G.; Endres, F. A Prussian blue/zinc secondary battery with a bio-ionic liquid–water mixture as electrolyte. *ACS Appl. Mater. Interfaces* **2016**, *8*, 12158–12164. [[CrossRef](#)] [[PubMed](#)]

39. Pu, X.; Jiang, B.; Wang, X.; Liu, W.; Dong, L.; Kang, F.; Xu, C. High-performance aqueous zinc-ion batteries realized by MOF materials. *Nano-Micro Lett.* **2020**, *12*, 152. [[CrossRef](#)]
40. Jiang, L.; Wu, Z.Y.; Wang, Y.; Tian, W.; Yi, Z.; Cai, C.; Jiang, Y.; Hu, L. Ultrafast zinc-ion diffusion ability observed in 6.0-nanometer spinel nanodots. *ACS Nano* **2019**, *13*, 10376–10385. [[CrossRef](#)]
41. Wang, X.; Xi, B.; Ma, X.; Feng, Z.; Jia, Y.; Feng, J.; Qian, Y.; Xiong, S. Boosting zinc-ion storage capability by effectively suppressing vanadium dissolution based on robust layered barium vanadate. *Nano Lett.* **2020**, *20*, 2899–2906. [[CrossRef](#)]
42. He, B.; Zhang, Q.; Man, P.; Zhou, Z.; Li, C.; Li, Q.; Xie, L.; Wang, X.; Pang, H.; Yao, Y. Self-sacrificed synthesis of conductive vanadium-based metal–organic framework nanowire-bundle arrays as binder-free cathodes for high-rate and high-energy-density wearable Zn-ion batteries. *Nano Energy* **2019**, *64*, 103935. [[CrossRef](#)]
43. Hu, P.; Yan, M.; Zhu, T.; Wang, X.; Wei, X.; Li, J.; Zhou, L.; Li, Z.; Chen, L.; Mai, L. Zn/V₂O₅ aqueous hybrid-ion battery with high voltage platform and long cycle life. *ACS Appl. Mater. Interfaces* **2017**, *9*, 42717–42722. [[CrossRef](#)]
44. Wang, J.; Wang, X.; Yu, J.; Xiao, T.; Peng, L.; Fan, L.; Wang, C.; Shen, Q.; Wu, W. Tailoring the grain size of Bi-layer graphene by pulsed laser deposition. *Nanomater.* **2018**, *8*, 885. [[CrossRef](#)] [[PubMed](#)]
45. Tan, K.; Liu, Y.; Tan, Z.; Zhang, J.; Hou, L.; Yuan, C. High-yield and in situ fabrication of high-content nitrogen-doped graphene nanoribbons@Co/CoOOH as an integrated sulfur host towards Li–S batteries. *J. Mater. Chem. A* **2020**, *8*, 3048–3059. [[CrossRef](#)]
46. Ding, L.; Gao, Q.; Yuan, C. Hierarchical CaMn₂O₄/C network framework toward aqueous Zn ion hybrid capacitors as competitive cathodes. *Batteries* **2023**, *9*, 586. [[CrossRef](#)]
47. Dai, J.; Zhu, C.; Fan, Y.; Wen, L.; Zhao, Y.; Huang, Z.; Zeng, W.; Wang, S. Zinc-ion supercapacitor with stress sensing function based on CZIF-67-CNTs cathode. *J. Energy Storage* **2024**, *83*, 110670. [[CrossRef](#)]
48. Peng, M.; Wang, L.; Li, L.; Tang, X.; Huang, B.; Hu, T.; Yuan, K.; Chen, Y. Manipulating the interlayer spacing of 3D MXenes with improved stability and zinc-ion storage capability. *Adv. Funct. Mater.* **2022**, *32*, 2109524. [[CrossRef](#)]
49. Gao, H.; Wang, J.; Zhang, R.; Wu, L.; Tao, C.; Deng, G. An aqueous hybrid lithium ion capacitor based on activated graphene and modified LiFePO₄ with high specific capacitance. *Mater. Res. Express* **2019**, *6*, 045509. [[CrossRef](#)]
50. Lu, K.; Li, D.; Gao, X.; Dai, H.; Wang, N.; Ma, H. An advanced aqueous sodium-ion supercapacitor with a manganous hexacyanoferrate cathode and a Fe₃O₄/rGO anode. *J. Mater. Chem. A* **2015**, *3*, 16013–16019. [[CrossRef](#)]

Disclaimer/Publisher’s Note: The statements, opinions and data contained in all publications are solely those of the individual author(s) and contributor(s) and not of MDPI and/or the editor(s). MDPI and/or the editor(s) disclaim responsibility for any injury to people or property resulting from any ideas, methods, instructions or products referred to in the content.